FEBS Letters

FEBS PRESS science publishing by scientists

RESEARCH ARTICLE

Modulation of Homer1 EVH1 domain internal dynamics by putative autism-associated mutations

Fanni Farkas[1], Brigitta Maruzs[1], Zsófia E. Kálmán[1], Tomas Klumpler[2], Gyula Batta[3], Bálint Péterfia[1] and Zoltán Gáspári[1]

1 Faculty of Information Technology and Bionics, Pázmány Péter Catholic University, Budapest, Hungary
2 CEITEC, Masaryk University, Brno, Czech Republic
3 Department of Organic Chemistry, University of Debrecen, Debrecen, Hungary

Correspondence
Z. Gáspári and B. Péterfia, Faculty of Information Technology and Bionics, Pázmány Péter Catholic University, Práter u. 50/A, 1083 Budapest, Hungary
Tel: +36 30 3329496 and +36 1 8864780
E-mail: gaspari.zoltan@itk.ppke.hu; peterfia.balint.ferenc@itk.ppke.hu

(Received 5 January 2026, revised 10 March 2026, accepted 8 April 2026, available online 28 May 2026)

doi:10.1002/1873-3468.70369

Edited by Christian Griesinger

The EVH1 domain of the Homer1 scaffold protein interacts with the proline-rich region of Shank3, forming a key network within the postsynaptic density. While two mutations (M65I and S97L) in the EVH1 domain have been suggested to be associated with autism spectrum disorder, our results show that neither mutation has a substantial effect on the overall structure or the partner binding properties of Homer1. Compared to the S97L variant, the M65I mutant exhibits larger chemical shift perturbations both upon the mutation itself and during partner binding, while also showing signs of thermal destabilization. Finally, integration of computational and NMR data suggests that both mutations perturb the µs-ms timescale internal motions of the EVH1 domain.

Keywords: chemical shift perturbation; hinge residues; HOMER1; postsynaptic density

Homer1 is the most studied member of the Homer family. It is a scaffold protein in the postsynaptic density (PSD), found beneath the postsynaptic membrane of central excitatory glutamatergic synapses [1]. The PSD is a complex structure with a high concentration of glutamate receptors, cell adhesion molecules, signaling enzymes, and cytoskeletal elements [2]. The PSD is a dynamically changing structure whose composition is different during response to synaptic activity, development, learning, and memory formation [3]. Pathological synapse development can contribute to different disorders (schizophrenia, mental retardation, Alzheimer's disease, and autism spectrum disorder) [3].

There are three mammalian genes encoding Homer1, 2 and Homer3. The cortical and CA1 hippocampal regions express mostly Homer1 which has 3 splice variants (Homer1a, Homer1b, Homer1c). Homer1c in PSD plays a crucial role in receptor clustering and trafficking, intracellular complex formation, and calcium homeostasis [1]. It interacts with proline-rich motifs in various proteins, such as mGluRs, actin, Oskar, RYRI, IP3Rs, Drebrin, and Shank/ProSAP/SAPAP [1,4–6]. This interaction is mediated by its N-terminal globular EVH1 [Enabled/vasodilator-stimulated phosphoprotein (Ena/VASP) homology 1] domain. Besides EVH1, it has a C-terminal coiled-coil segment and a 77-residue long disordered region between them. EVH1 has 7 beta strands and a C-terminal alpha helix (Fig. 1). EVH1 forms an interaction with consensus sequences FPxoP and PPxxF

Abbreviations
ASD, autism spectrum disorder; BLI, biolayer interferometry; BMRB, Biological Magnetic Resonance Data Bank; CD, circular dichroism (spectroscopy); CEST, chemical exchange saturation transfer; CSP, chemical shift perturbation; EVH1, Ena/Vasp Homology domain 1; GNM, Gaussian Network Model; MD, molecular dynamics; NMR, nuclear magnetic resonance (spectroscopy); NOE, nuclear overhauser effect; PDB, Protein Data Bank; PSD, postsynaptic density; RMSF, root mean square fluctuation; SAXS, small-angle X-ray scattering; SDS/PAGE, sodium dodecyl sulfate/polyacrylamide gel electrophoresis; TSA, thermal shift assay.

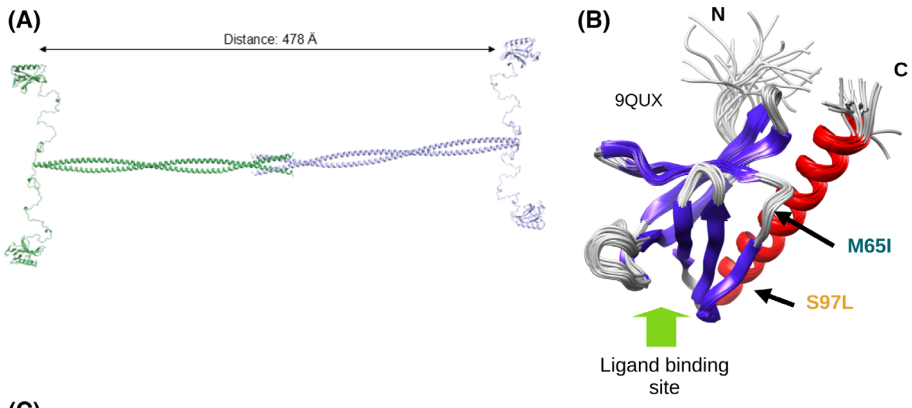

Fig. 1. Overview of the structure of the Homer1 molecule and its EVH1 domain. (A) Architecture of the full-length Homer1 tetramer (model from Kálmán et al. 2025, [8]). (B) Solution structure of the Homer1 EVH1 domain (PDB ID: 9QUX). The ligand-binding site, as well as the positions of the M65I and S97L mutations, are indicated. Figure prepared with ChimeraX. (C) Sequence of the Homer1 EVH1 domain with the secondary structure elements and the mutations highlighted.

[5,7]. Homer1c binds its ligands by Gly89, Val85, Gln76, Phe74, Thr70, and Trp24 amino acids.

Our previously determined solution structure of the wild-type (WT) EVH1 domain (PDB ID: 9QUX) exhibits high overall similarity to the other available EVH1 structures and shows excellent agreement with SAXS measurements [8]. However, it exhibits subtle conformational differences relative to X-ray structures in several loop regions, including regions 17–29 and 40–43, involved in partner binding. In addition, in the NMR structure, the indole ring of Trp24 adopts a nearly perpendicular orientation relative to the Homer1 EVH1 crystal structures (1DDV and 1DDW) [5], suggesting a possible reorganization of the key aromatic cluster (Phe14, Trp24, and Phe74) during partner binding. These findings highlight the structural plasticity of the binding site and its potential role in accommodating diverse pro-rich ligands [8].

Shank is one of the interaction partners of Homer1c. It is a multidomain synaptic scaffold protein [9]. Starting from the N-terminal depending on the alternative splicing, Shank proteins possess an ankyrin repeat region, an SH3 domain, and a PDZ domain which is the main interaction partner in Shanks and participates in the NMDA-PSD-95-GKAP-Shank complex. Besides, Shank has a long disordered proline-rich domain that interacts with the EVH1 domain of the Homer protein. Lastly, it has a C-terminal SAM domain.

The Homer-binding motif, containing the consensus PPxxF, is different in the known Shank paralogs. In Shank1, its sequence is PLPPPLEFSN; in Shank2, there are two putative sites: PLPPPLEFAN and FLPPPESFDA; and in Shank3, the sequence is LVPPPEEFAN [10].

The SHANK3 gene was identified as an autism spectrum disorder (ASD) risk gene and was recently found to be one of the most frequent causes of ASD [9].

Autism spectrum disorder is a neurodevelopmental disability condition in early childhood affecting 1% of the children [11,12]. It is associated with repetitive behavior, impaired communication and social interaction, and a limited range of interests [12,13]. In relation to ASD copy number variants (CNVs) and mutations in individual genes have been documented [12]. Homer1 has been linked to multiple neurological disorders, such as Alzheimer's disease, schizophrenia, and others, including ASD [1,14]. The HOMER1 gene was identified as a novel autism-risk gene. Homer1 participates in the downstream mGluR signaling, alteration in this pathway contributes to nonsyndromic autism [12]. In the HOMER1 gene, five missense point mutations (M65I, S97L, P142L, R323H, and 3′UTR)

FEBS Letters **600** (2026) 2307–2319 © 2026 The Author(s). *FEBS Letters* published by John Wiley & Sons Ltd on behalf of Federation of European Biochemical Societies.

were reported, based on the sequence, M65I and S97L (DNA: 195G>T resulted M65I and DNA: 290C>T resulted S97L) found in the EVH1 domain of Homer1 (Fig. 1C) [12]. To our knowledge, the effect of the mutations on the structure and function of the EVH1 domain has not yet been investigated.

In our previous study, complete backbone and partial sidechain NMR chemical shift assignments were obtained for the WT EVH11–118 domain. In this study, to explore the effect of putative ASD-related mutations, we report the expression, purification and resonance assignment of two murine Homer1 EVH1 mutant (M65I and S97L) domain constructs. We present the analysis of the backbone dynamics and the partner binding properties of these variants and compare these to each other and the WT EVH1 domain. Using NMR and CD spectroscopy, SAXS, thermal shift assay, biolayer interferometry and molecular modeling, our integrated analysis suggests that the mutations primarily affect the characteristic internal dynamics of the domains rather than their overall structure or ligand binding at the canonical site.

Materials and methods

Cloning, protein expression and purification

After successful production and purification of the WT Homer1 EVH1 protein, using the segment 1–118 from *Mus musculus* (UniProt ID: Q9Z2Y3) (see details in our previous article: [8]), two autism-associated point mutations, M65I and S97L, were introduced in its sequence with *in vitro* PCR mutagenesis. Proteins were expressed in BL21 (DE3) *Escherichia coli* bacterial cells (Novagen) in unlabeled and ^{15}N and ^{15}N, ^{13}C labeled forms as well. For unlabeled, LB medium was used. For isotopically labeled protein freshly prepared M9 medium was used [15] supplemented with 0.2× Trace element mix [16], 2.5 g·L^{-1} $^{15}NH_4Cl$ (Cambridge Isotope Laboratories, Cambridge, MA), and 4 g·L^{-1} unlabeled glucose or [^{13}C]-D-glucose in the case of double labeled version. With ultrasonic homogenization (30 min, 30% pulse, 30% power) the bacteria cell wall was destroyed. To make the protein of interest available, the following purification steps were used; first, IMAC was performed using a 5 mL Bio-Scale™ Mini Nuvia™ IMAC Ni-affinity column (Bio-Rad). This column binds the His-tag in the target protein; therefore, with a washing step, other unbounded proteins can be rid of. To cleave the His-tag from the protein of interest, TEV protease was added. The second purification step was the Ion Exchange Chromatography by using the Bio-Scale™ Mini Macro-Prep® High S column. With a reverse IMAC step, the cleaved His-tags were eliminated from the target protein. Sample was concentrated (~9 mg·mL^{-1}), and finally, to get an NMR compatible pure sample without any additional contamination, a third purification step was applied and size exclusion chromatography by using the SEC70 analytical gel chromatographic column (Bio-Rad). The recombinant EVH1 proteins were eluted in the NMR compatible low salt NaPi buffer (50 mM NaPi; 20 mM NaCl, 0.02% NaN_3; pH 7.4) and concentrated again for NMR measurement. To determine its purity and molecular weight, sodium dodecyl sulfate/polyacrylamide gel electrophoresis (SDS/PAGE) and NanoDrop2000 were used.

Molecular mass of the protein constructs was analyzed by HPLC-MS using a Shimadzu LC–MS-2020 device equipped with a Reprospher-100 C18 column and a positive–negative double ion source (DUIS±). A quadrupole MS analyzer in a range of m/z 50–1000 was used. For gradient elution, 0.1% formic acid in water (as eluent A) and 0.1% formic acid in acetonitrile (as eluent B) were used.

Biolayer interferometry (BLI)

Streptavidin biosensors (Sartorius) were hydrated in a kinetic buffer (50 mM NaPi pH 7.4, 20 mM NaCl, 1% BSA, 0.1% Tween 20) at 25 °C for 10 min before the experiments. The concentration of Tween 20 and BSA in this buffer was increased to 0.1% and 1%, respectively, in order to minimize the strong aspecific binding of the mutant EVH1 constructs to the biosensor. Kinetic assays were performed using a BLItz system (ForteBio, USA). Biotinylated Shank3 peptide ligand (BioBasic, Toronto, CA) with the sequence LVPPPEEFANG (corresponding to residues 1381–1391 of UniProt entry Q9BYB0 representing human Shank3 but also occurring with identical sequence in the mouse and rat Shank3 proteins) was anchored to the biosensor surface for 60 s at 2 mM concentration. For reference, only the kinetics buffer was added for 30 s. Five different EVH1 analyte concentrations (~10-, 5-, 2,5-, 1.25-, and 0 μM) were used for the 30 s long association step of the runs. The equilibrium dissociation constant (Kd) was determined from the BLI data using the data analysis software's global fitting method. For reference, the curve with 0 μM analyte was used.

Thermal shift assay

The thermal shift assay (TSA), also known as differential scanning fluorimetry (DSF), was used by rtPCR (PikoReal2 qPCR; Thermo Scientific) to determine thermal denaturation of the unbound and peptide-bound WT and mutant EVH1 domains. It detects fluorescence changes from a dye (SYPRO Protein Gel Stains; Thermo Scientific) that forms a binding with the hydrophobic region upon unfolding. It is a technique widely used to study protein stability and ligand binding because of its simplicity, low sample requirement, and high-throughput capability. Melting temperature

(Tm) shifts indicate the stabilizing or destabilizing effect of a ligand or environmental condition on the protein [17]. For TSA measurement, 0.375 mg·mL^{-1} protein (WT, M65I, and S97L), 186 mM Shank3 peptide (BioBasic, Toronto, CA), and 5× SYPRO were used. As a protocol setting temperature was increased from 25 Celsius degree to 90 with 12 s hold time, temperature increment after hold 0.3 °C.

ECD spectroscopy

Far-UV CD spectroscopy measurement was performed with JASCO J-1500 CD spectrometer (JASCO Corporation, Tokyo, Japan) in the 195–250 nm spectral range, 50 nm·min−1 scanning speed, 1 nm bandwidth, 0.2 nm step size, 0.5 s response time, and 3 scans of accumulation and baseline correction. It was recorded in a 1-mm pathlength cuvette (J/21 quartz). Sample concentrations were 10 μM in 50 mM NaPi, 20 mM NaCl, pH 7.4 buffer. In order to check temperature dependence, the 20 °C–60 °C interval was used; measurements were done at 10 degree steps.

Small-angle X-ray scattering measurements

Samples containing the M65I and S97L mutant EVH1 domains were prepared as described above but without isotope labeling. The concentrations for the SAXS measurements were set to 4 and 2 mg·mL^{-1}. SAXS measurements were performed on a Rigaku BioSAXS-2000 instrument at CEITEC (Brno, Czech Republic), equipped with a HyPix-3000 detector, at a sample-to-detector distance of 0.48 m. The scattered intensity was recorded over a q-range of 0.008–0.65 Å^{-1}, where $q = 4\pi\sin\theta/\lambda$, 2θ is the scattering angle, and $\lambda = 1.54$ Å. Six frames of 10 min each were collected at a sample temperature of 25 °C. The raw data were normalized to the intensity of the transmitted beam and radially averaged. Each individual frame was inspected for radiation damage prior to averaging. Finally, the scattering contribution of the solvent blank was subtracted to obtain the sample scattering profile. Structure-based calculation of SAXS curves was performed with Pepsi-SAXS [18] using the structural models built based on the WT structure after equilibration (see the molecular dynamics calculation section below) containing the expression tags (GSH) at their N terminus to properly reflect the samples actually used for the measurements.

Nuclear magnetic resonance measurements

All experiments were performed on a Bruker Avance NEO 700 MHz spectrometer at 298 K. For the resonance assignment of the M65I and S97L variants, 500 μL samples containing 50 mM sodium phosphate buffer, 20 mM NaCl, 0.02% NaN_3 at pH 7.4 with 6% D_2O were used with protein concentrations of 491 μM for the M65I and 560 μM for the S97L variants, respectively. ^{15}N-^{1}H HSQC, ^{13}C-^{1}H HSQC as well as standard triple-resonance spectra were recorded: HNCO, HN(CA)CO, HNCA, HN(CO)CA, HNCACB and HN(CO)CACB. HCCH-TOCSY, HCCCONH. NMR spectra were processed in Bruker TopSpin, and analysis was performed in CCPNMR v3.2.3 [19] and NMRFAM-Sparky 1.413 [20]. Neighbor-dependent secondary chemical shifts were calculated by the method described by Tamiola et al [21] as included in the CoNSEnsX$^+$ server [22].

For backbone ^{15}N relaxation measurements, ^{15}N labeled samples were used, containing 207 μM protein for the M65I and 228 μM for the S97L variant. Standard Bruker pulse sequences in pseudo3D implementation were used. The delay times were 40, 80, 120, 160, 200, 300, 400, 600, 1200, and 2400 ms for T_1 and 1, 2, 3, 4, 5, 6, 7, 9,12, 15, and 18 cycles of a 16.96 ms loop (from the parameters p30 and d21 in the Bruker pulse sequence) for T_2 measurements. For these experiments, a delay time (D1) of 4 s was used. ^{1}H-^{15}N heteronuclear NOE was measured in an interleaved fashion with a delay time of 8 s. The obtained spectra were first processed with TopSpin. Peak intensity calculation and curve fitting was performed with NMRFAM-Sparky 1.413 [20]. For model-free analysis, the program Tensor2 was used [23]. Cross-peaks exhibiting substantial overlap were excluded from the estimation of the correlation time and model-free analysis. The rotational correlation time was estimated using data only for residues with T_1/T_2 values within 1 standard deviation of the average. The analysis was performed to ensure compatibility with our earlier investigation of the WT domain [8].

To explore possible phenomena associated with slow-timescale dynamics in more detail, ^{15}N CEST measurements [24] were performed on ^{15}N labeled samples for both mutants plus the WT EVH1 domain. The delay time was 1 s and the irradiation time was set to 4 s. Initial analysis of the data was conducted using ColmarVista [25]. As no clear effects were detected upon visual inspection of the peak intensities, no further analysis of these data was performed.

NMR titration of the ^{15}N-labeled WT1–118 (571 μM), M65I1–118 (509 μM), and S97L1–118 (352 μM) Homer EVH1 was performed with a short Shank3 peptide (BioBasic, Toronto, CA) corresponding to the immediate binding motif (LVPPPEEFANG) (+ 10 μL / 4.5 mM peptide/titration point). Ten titration points were measured, and the points closest to 1 : 1 stoichiometry were selected for comparison of the variants. Data were analyzed using CCPNMR v3.2.3 [19].

Amide NH chemical shift perturbations observed for the mutants and upon titration with the Shank3 peptide were calculated using the formula $CSP = \sqrt{0.14 * \Delta\delta N^2 + \Delta\delta H^2}$.

Computational structure modeling and analysis

For molecular dynamics calculations, the initial WT structure was derived from the first (representative) model of

our previously determined Homer1 EVH1 NMR structure (PDB ID: 9QUX). Mutations were introduced with FoldX [26]. Molecular dynamics simulations were performed with GROMACS (version 2023.2) [27] using explicit solvent classical MD. Three parallel simulations for the WT and the two mutant domains were performed. AMBER99SB-ILDN [28] was used as a force field. During the simulation the box setting was a minimum distance of 1.0 nm from the box edge. Two rounds of equilibration were performed using 1 ns simulations with position restraints on the heavy atoms, first using volume coupling (NVT ensemble) and then temperature coupling (NPT ensemble). From the 1 ms production run, 500 snapshots were taken. Computations were performed on the Komondor supercomputer. RMS fluctuations were calculated with GROMACS rmsf command. Secondary structure of the models was analyzed using DSSPcont [29]. Noncovalent interactions were analyzed using RING [30].

Gaussian network model analysis was performed using Prody [31] on a model of the WT protein from which the expression tag was removed and renumbered accordingly. Structure visualization was done with ChimeraX [32]. Python3 was used for further data processing and Gnuplot and MSOffice Excel for data visualization.

Human EVH1 sequences were downloaded from Interpro [33] and sequences aligned in Jalview [34] using ClustalO [35]. Orthologous sequences were downloaded from OMA [36].

Results and discussion

^{1}H-^{15}N HSQC spectra indicate different effects of the mutations

Throughout this work, we use the residue numbering corresponding to the UniProt entry Q9Z2Y3. We note that relative to this, the numbering of our previously deposited Homer1 EVH1 NMR structure (PDB ID: 9QUX) is shifted by 3 residues due to the presence of the remnants of the expression tag.

The S97L and M65I variants of the Homer1 EVH1 domain could be successfully expressed using the protocol applied for the WT domain. Polyacrylamide gel electrophoresis and mass spectrometry measurements indicate that the obtained samples conform to the expected molecular mass of the variants. NMR resonance assignment could be completed for both mutants with over 87% completion for backbone atoms. Chemical shifts along with ^{15}N relaxation data have been deposited in the BMRB with IDs 53 479 (M65I) and 53 480 (S97L). In general, most of the amide peaks of the S97L variant align well with those of the WT EVH1 domain, while for the M65I variant, the ^{1}H-^{15}N HSQC spectrum indicates the alteration of the chemical environment for the majority of the residues (Fig. 2A). For both mutants, amide cross-peaks of the residues in and near the mutated positions show marked alterations. In the case of the M65I mutant, the affected region is longer, with some residue positions in the segment 60–78 exhibiting larger chemical shift perturbations. This observation suggests that the effect of the two mutations is profoundly different and prompted further investigations on the structures of the two variants (Fig. 2B, Fig. S1A).

The overall structure of the mutated EVH1 domains is largely unaltered

Both circular dichroism spectroscopy and small-angle X-ray scattering experiments indicate that neither of the mutants exhibits a structure substantially different from that of the WT domain. This was confirmed by fitting the SAXS curves to the structural models built based on our previously determined EVH1 structure. The χ^2 value of the fit for the M65I variant is 1.12 and 1.10 for the S97L mutant (Fig. 2C). SAXS results have been deposited in the SASBDB database with IDs SASDYW3 (M65I) and SASDYX3 (S97L). Analysis of the secondary Cα and Hα chemical shifts also confirms that the secondary structure elements remain largely the same relative to the WT domain (Fig. 2D). In addition, a number of characteristic amide NH-NH NOE cross-peaks expected based on the NMR structure of the WT domain (PDB ID 9QUX) are present in the 3D NOESY-HSQC spectra of the M65I variant (Fig. S1B). These data strongly suggest that the observed chemical shift perturbations are not due to a substantial structural rearrangement upon mutation of the M65 residue. This also means that the observed chemical shift changes should be interpreted in the framework of the characteristic EVH1 structure (Fig. S2), and the explanation of the differences might lie beyond the static average structures. Therefore, we set out to explore the thermal stability and internal dynamics of the mutants in more detail.

The M65I variant shows thermal destabilization and a markedly two-step unfolding kinetics

The stability of the EVH1 domain variants was investigated by thermal shift assay experiments. Interestingly, all three variants investigated—the WT, S97L, and M65I mutants—exhibit two transition temperatures, but the lower one of these is indicated only by a relatively small peak in the case of the WT and the S97L mutant (Fig. 3A). Surprisingly, the S97L variant shows a slightly decreased first but an elevated second

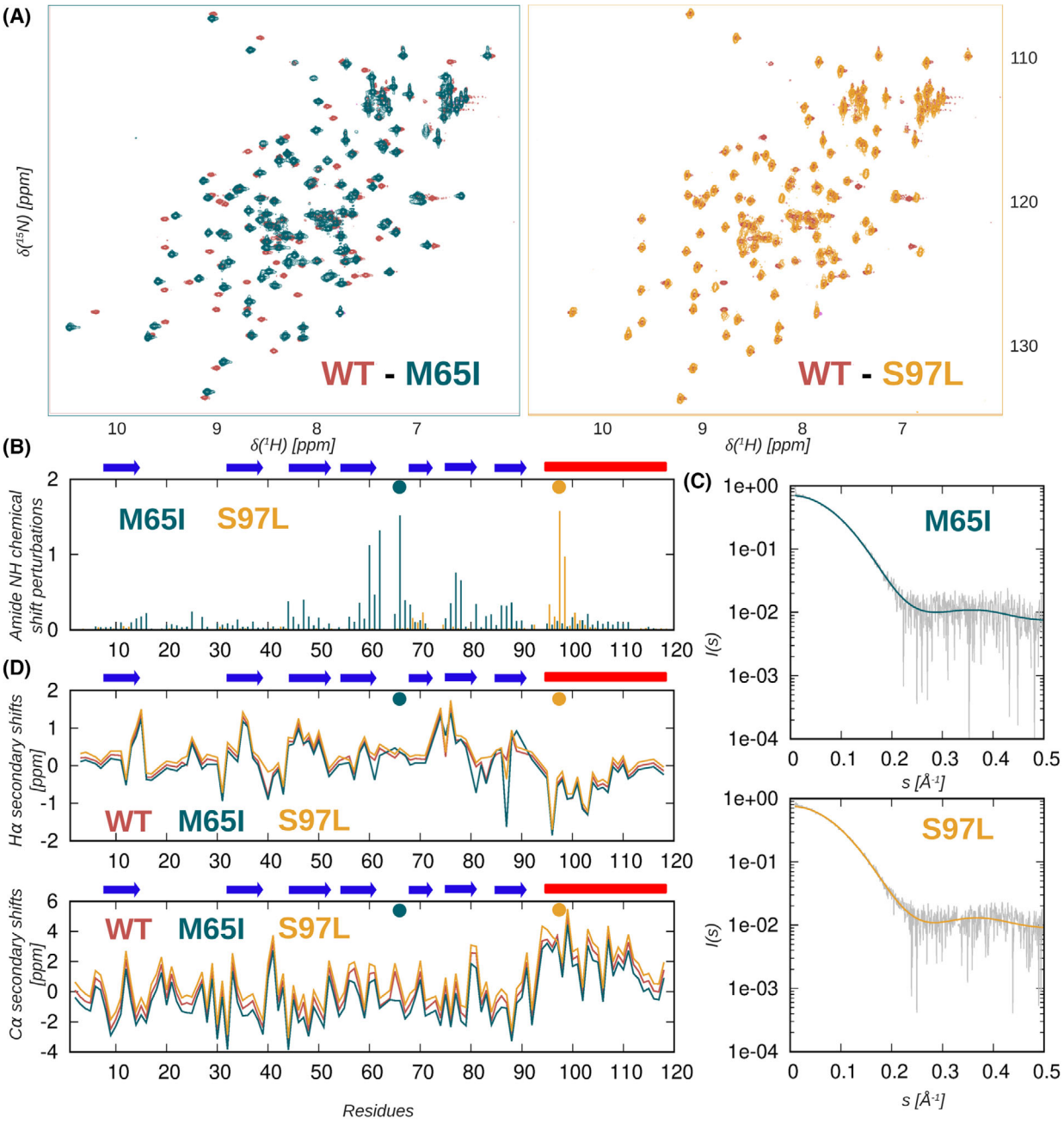

Fig. 2. Structural analysis of the EVH1 domain variants investigated. (A) Overlaid ^{1}H-^{15}N HSQC spectra of the mutant EVH1 domains with the wild-type (WT). Peaks are color-coded as indicated. (B) Amide NH chemical shift perturbations (CSPs) for the two mutants along the sequence. CSPs were calculated as: $\sqrt{0.14 * \Delta\delta N^2 + \Delta\delta H^2}$. (C) SAXS fits to structural models of the mutants built based on the WT and having essentially the same overall structure. The experimental curves are shown in gray, those calculated for the structural models in color. (D) Secondary Hα and Cα chemical shifts of the WT and mutant variants. The interconnecting lines are only shown for visualization purposes to emphasize the similar trends in the data. Data for the mutants are slightly shifted upward and downward to reduce the overlap of the lines and aid better visualization. Data for the WT are from [8] (BMRB entry 34 990). On panels B and D, the positions of the mutations are denoted with dots colored according to the color scheme of the legend, and the approximate positions of the regular secondary structure elements are also indicated (blue: *β*-strands, red: *α*-helix).

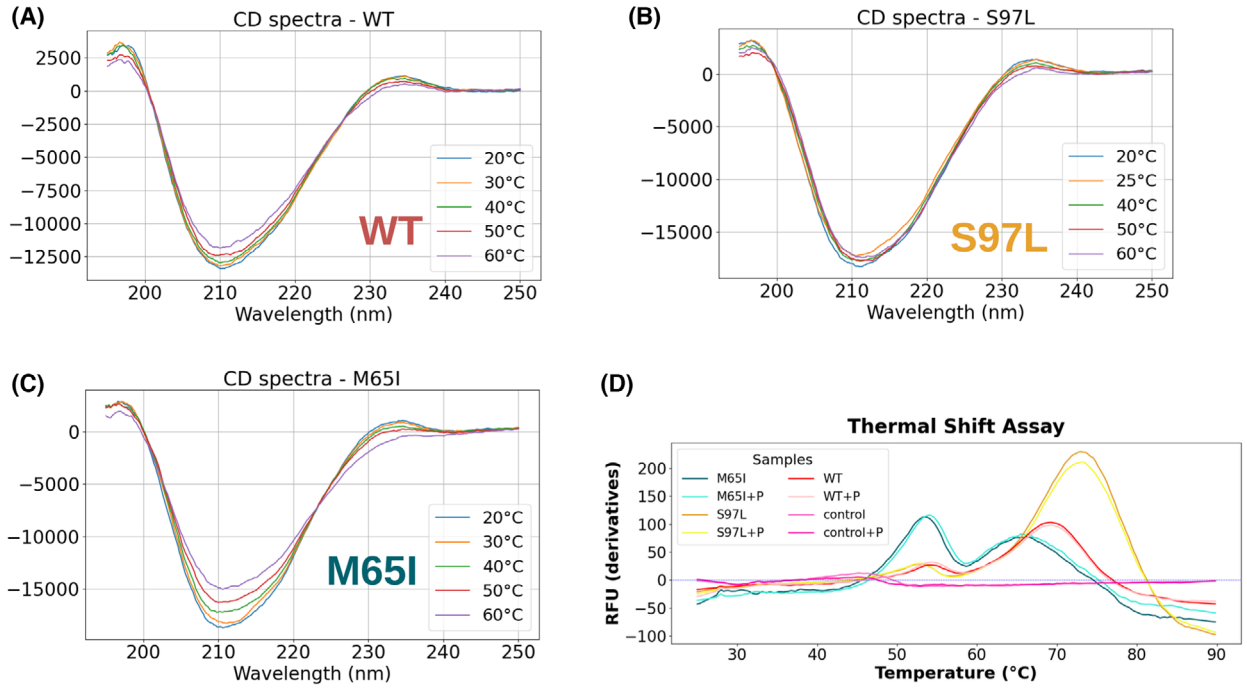

Fig. 3. Temperature dependence of the structure of the EVH1 variants. (A) Thermal shift assay curves for all three variants with and without ligands. Average curves from duplicate measurements are shown. (B) Wild-type (WT), (C) M65I, and (D) S97L variants. The spectra for the WT were taken from our previous work [8].

transition temperature compared with the WT domain. In sharp contrast, the melting curves for the M65I variant exhibit a higher peak at the first and a smaller peak at the second transition that occurs at a lower temperature than for the WT domain.

Intriguingly, binding to the Shank3 peptide causes only subtle alterations in the melting curves, indicating that the interaction does not cause any noticeable stabilization or destabilization.

Circular dichroism spectra do not indicate the presence of any substantial structural changes at higher temperatures, with the highest alterations observed again for the M65I variant (Fig. 3B–D).

NMR spectroscopy suggests somewhat different conformational response to ligand binding in the mutants

We tested the ability of the variants to bind a partner peptide derived from Shank3. Biolayer interferometry measurements indicated that the mutants bind the peptide with a comparable affinity to that of the WT domain, with S97L showing a slightly stronger and M65I a slightly weaker binding (Table 1 and Fig. 4A). Even so, the difference between the strongest binder, S97L, and the weakest, M65I, is still only approximately twofold, indicating that the overall strength of the binding is not substantially affected by the mutations.

We have also explored the response of the domain variants to peptide binding by NMR spectroscopy. As expected, a number of amide cross-peaks corresponding to residues near the ligand-binding site exhibit changes in their position in the ^{1}H-^{15}N HSQC spectra (Figs 4B, S3 and S4). Although the overall pattern is largely similar in all three variants, the M65I mutant exhibits generally larger changes than the WT and S97L (Fig. 4B).

^{15}N relaxation analysis suggests the presence of distinct slow-timescale motions in the variants

To explore the internal dynamics of the mutant EVH1 domains, ^{15}N relaxation measurements were performed and evaluated with model-free analysis (Figs 4C and S5–S7). The results were compared with our previous analysis of the WT domain. Interestingly, residue Asn23 in the ligand-binding site exhibits a heteronuclear NOE value above 1 in all three variants, as do some terminal residues. These were excluded from the final model-free analysis. For Asn23, an internal residue, this phenomenon is worth noting as it might

Table 1. Binding affinity of the variants to the Shank3 peptide as determined by biolayer interferometry.

Variant	WT	M65I	S97L
Global Kd [μM]	5.15	8.88	3.88
R^2 (coefficient of fit)	0.99	0.99	0.98

indicate complex dynamical behavior for this residue. Backbone S^2 order parameters of the mutants align generally well (Figs 4C and S7) with those determined for the WT domain. The obtained model-free fits were in some cases regarded as unreliable, either with very high (>1) S^2 or S^2f values and/or no robust fit to either of the motional models in Tensor2. However, most of the affected residues are in the terminal regions where increased mobility is expected. In the core of the domain, the largest difference relative to the WT occurs in the segment between residues 19–25 where, in the case of the M65I mutant, two asparagine residues, Asn19 and Asn23, have lower S^2 values than the WT and/or the S97L variant (Figs 4C and S7). Interestingly, in S97L, Lys21 is fitted with an S^2 of 1. These residues are very close to the ligand-binding site, and it is notable that the two mutants show opposite changes in their ps-ns timescale dynamics in this region. However, the largest difference in the internal dynamics of the variants is the different distribution of residues with a fitted R_{ex} contribution (Figs 4C and S8), also apparent in their R_2 relaxation rates. Somewhat subjectively, we have defined a threshold of 2.5 Hz above which we consider the R_{ex} contributions substantial, but for most of the cases discussed below, the observed differences between the variants do not largely depend on this choice. Most notably, both the M65I and S97L mutants exhibit an altered pattern of affected residues near both mutation sites. All three variants seem to retain the cluster of residues with a large Rex contribution in the N-terminal region of the *α*-helix, albeit with slight alterations near residue 97. The residue Leu97 of the S97L mutant shows a large R_{ex} contribution, but not Ser97 in the WT and M65I variants. Similarly, Ile65 has relatively large R_{ex} only in the M65I mutant, but nearby residues in strand *β*5 are differently affected in all three variants. We note that although our analysis suggests that residue Thr70 only exhibits a substantial R_{ex} contribution in the mutants, its cross-peak exhibits a large R_2 relaxation rate also in the WT domain, but we have excluded it from our final published analysis [8] due to resonance overlap. In the N-terminal half of the domain, residues Asp39 and Val44 have R_{ex} above 2.5 Hz only in the WT EVH1 but not in any of the mutants. The pattern close to the N terminus is variant-specific: Val25 is affected only in the WT and the S97L mutant, whereas a cluster of residues in the region 14–16 shows differently distributed high R_{ex} values in all three variants, with variations in which residues exhibit R_{ex} above or threshold of 2.5 Hz (Figs 4C and S8).

To analyze the presence of slow-timescale motions in more detail, CEST experiments were also conducted; however, these did not provide conclusive results, indicating that the differences are likely solely related to internal motions with an exchange rate faster than 200 s^{-1} [24].

Molecular dynamics analysis supports experimental observations

Multiple rounds of molecular dynamics simulations were run on the free state of WT and the mutant versions of the domain. On the investigated timescale (1 microsecond) no major differences were observable between WT and mutants. RMSF values are comparable between the different structures, except for a small deviation in the loop connecting ß1 and ß2 (Fig. S9). Only terminal mobility and loop flexibility appear in the modes, and the rest of the structure seems to be unaffected (also observable in the initial and final models generated from MD trajectories) (Fig. S10). This is in line with the inferred secondary structures, which show that the domains seem to be stable and unaltered by the mutations in general. Some variability can be seen not in the positions containing mutations, but in their vicinity; but this does not significantly affect the assigned secondary structures. The same applies to residue contacts as well, where we see minor variations in van der Waals interactions and H-bond patterns in the mutants, but not in the exact positions of the substitutions.

Gaussian network model analysis of the EVH1 domain identifies hinge residues with experimentally supported role in dynamics and ligand binding

We have estimated the distribution of slow internal motions in the EVH1 domain structure using the Gaussian Network Model (GNM) formalism as implemented in ProDy [31]. This simplified model takes only C*α* positions into account; thus, this analysis is not suitable to reveal any differences in the mutants with the same overall structure, as in the present case. However, comparing the GNM results, revealing general features of the EVH1 architecture, with position-specific data obtained from NMR experiments, that

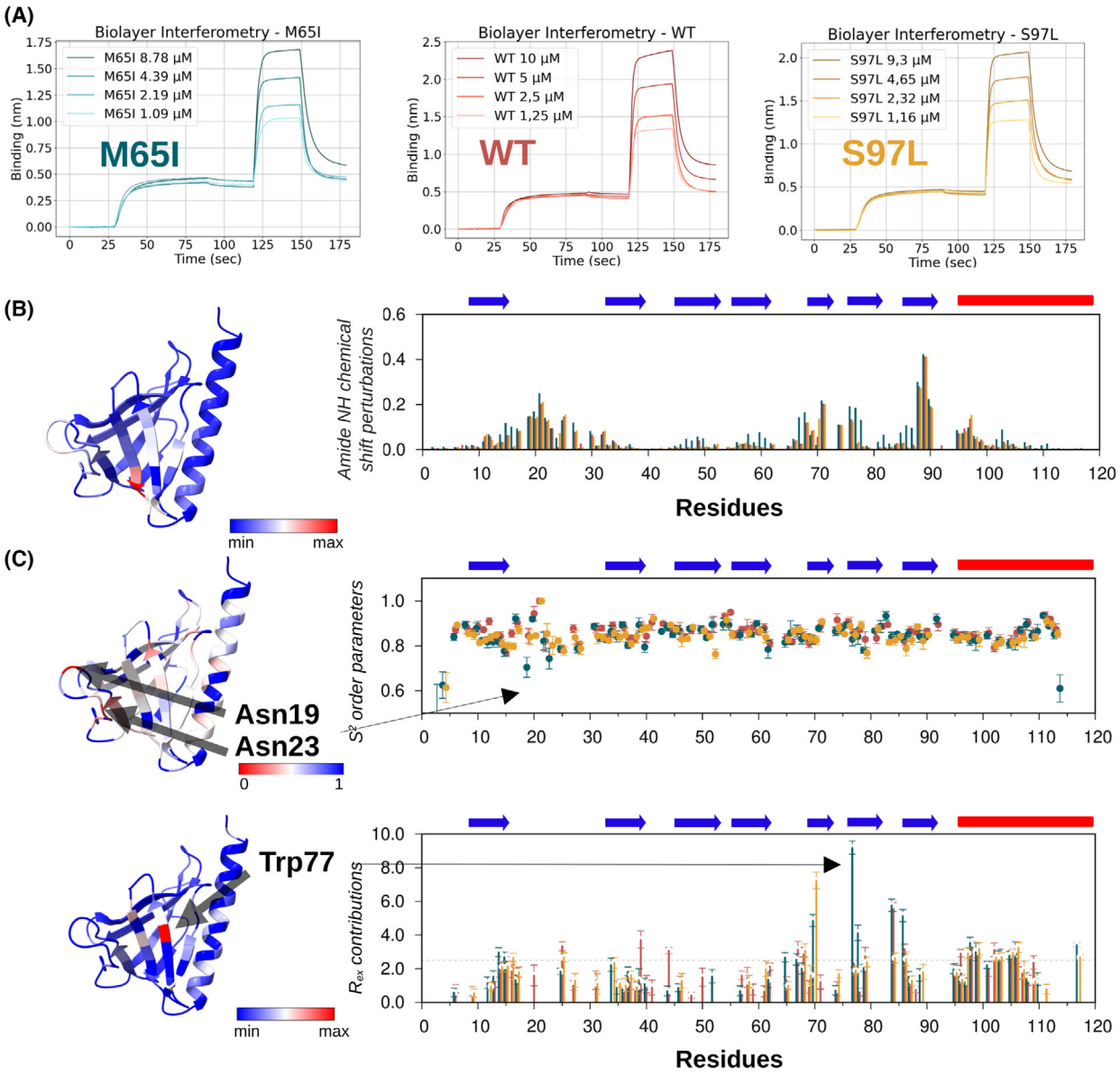

Fig. 4. Ligand binding and internal dynamics of the EVH1 variants investigated. (A) Biolayer interferometry assay probing the binding of the EVH1 domain variants to the Shank3 peptide. (B) Amide NH chemical shift perturbations observed upon ligand binding for the variants. CSPs were calculated as: $\sqrt{0.14 * \Delta\delta N^2 + \Delta\delta H^2}$. The structure on the right is colored according to the changes in the M65I variant. (C) S^2 backbone order parameters and fitted R_{ex} values of the variants investigated. Error bars represent the error of the parameter fitting estimated by Tensor2. Structures on the right show residues with notable differences to the wild-type (WT) in the M65I mutant. To highlight the lowest relevant S^2 values on the structural model outside the termini, the color range was applied between 0.7 and 1.0 with lower values uniformly colored red. Data for the WT are from [8] (BMRB entry 34 990). Structure depictions prepared with ChimeraX. Above the diagrams in B and C, the approximate positions of the regular secondary structure elements are also indicated (blue: β-strands, red: α-helix).

are, by their nature, highly sensitive to the changes of the chemical environment of the individual residues, has the potential to reveal relevant clues on the mechanistic effects of the mutations.

The first two modes identified by GNM suggest that the 'upper' and 'lower' parts of the domain can move relative to each other (Fig. 5A). Somewhat surprisingly, the sets of hinge residues for these modes are

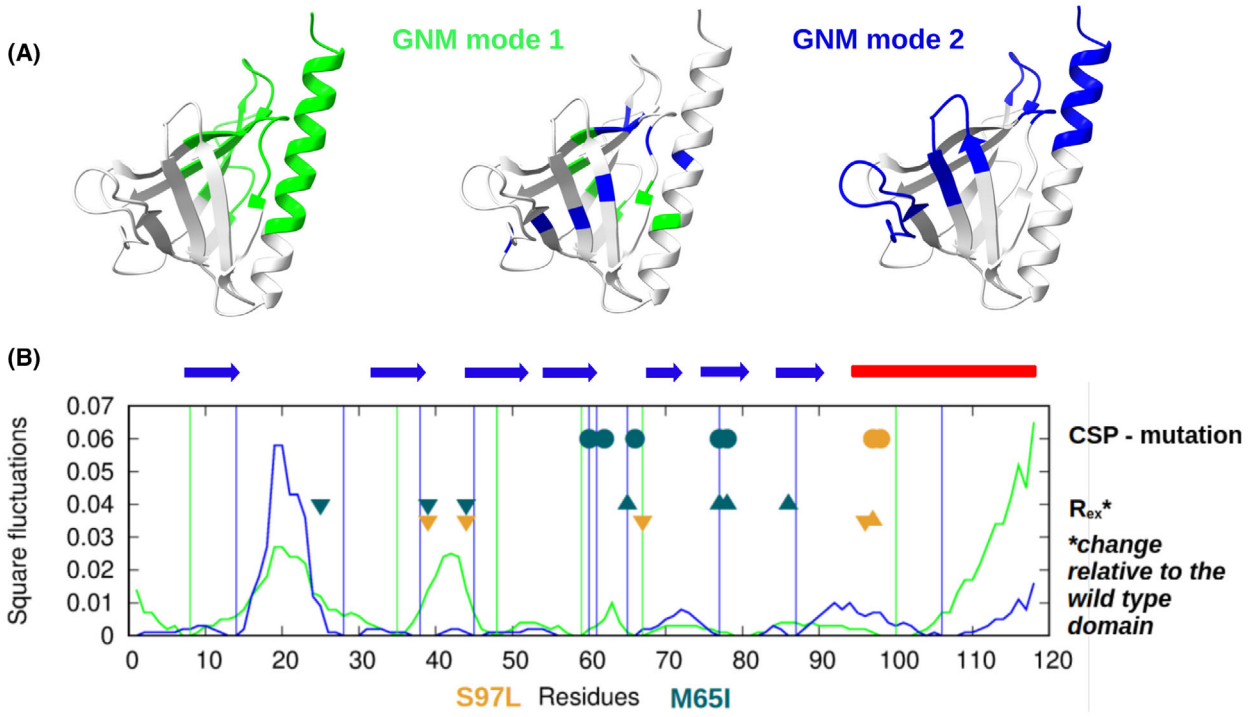

Fig. 5. Gaussian network model analysis of the EVH1 domain architecture. (A) In the structural models, the upper part of the structure for partitionings (left and right) according to the modes, as well as the hinge residues colored green for Mode 1 and blue for Mode 2. The structural depictions were created with ChimeraX. (B) Square fluctuations along the first and second modes shown along the sequence with green and blue lines, respectively. Vertical lines denote the positions of the hinge residues of the modes. Circles show the residues with substantial chemical shift perturbation relative to the wild-type (WT) domain. Triangles indicate sites with changes in substantial R_{ex} contributions relative to the WT, symbols pointing downward for decrease, those pointing upward for increase in the R_{ex}. Sites are only shown where the change causes a transition to/from a large Rex (> 2.5 Hz) and the change itself exceeds 1 Hz. Symbols colored according to the mutants as shown in the key. Above the diagram, the approximate positions of the regular secondary structure elements are also indicated (blue: β-strands, red: α-helix).

largely located within well-defined secondary structure elements, notably, in the beta-sheets and also near the middle of the α-helix. Notably, there is a short stretch between Residues 59 and 67 that contains hinge residues for both modes, residue Met65 itself being identified as a hinge for Mode 2. Even if the GNM modes only approximately describe the actual motions of the domain, it is very likely that the M65 mutation affects a residue that is part of a segment that plays a key role in both of the first two major motional modes. This is also supported by the distribution of the residues with the largest CSP and/or changes in fitted R_{ex} values in the M65I mutant, a number of which—Thr60, Thr66, Trp77 for CSP, Phe14, Met65, and again Trp77 for R_{ex} contributions—correspond to hinge sites for Mode 2 in the GNM analysis. Interestingly, several sites near Mode 2 hinges have altered R_{ex} contribution in both mutants, namely, Asp39 and Val44, located in the hairpin flanked by hinge sites Tyr38 and Tyr45. For the S97L variant, the observed pattern is less in line with the GNM results, as residue Leu97, exhibiting both a large CSP and an increased R_{ex} in the mutant, is not clearly associated with a hinge region, the closest position being residue 100, a hinge in Mode 1 and located almost a full turn away in the helix, facing inward (Fig. 5B).

Possible functional consequences of the mutations

In the InterPro database, EVH1 domains show substantial variability in the positions corresponding to the mutations M65 and S97. For M65, multiple hydrophobic amino acids occur in the various domains, but Ile is not present in this position. In the case of S97, a larger range of residues can be observed, consistent with the exposed nature of the residue (Fig. S11). Interestingly, although this position is highly conserved, Thr can also occur beside Ser; but more importantly, in some fish species, Leu can also be found in

this position. These observations suggest the presence of a functional rather than structural constraint for these positions (Fig. S11).

Our analysis, largely based on NMR spectroscopic data, suggests that the mutations do not alter the overall structure of the domain; rather, they affect its internal motions on a well-defined timescale. The nature of these motions is not exactly clear, but the distribution of the hinge residues suggests that the domain remains largely compact and that the residue displacements are of moderate amplitude. The two largest motions identified by GNM divide the domain into upper and lower parts, the lower part (in the orientation of our usual depiction) containing the ligand-binding site. Although GNM does not yield information on the direction of the motions in terms of vectors, it just reports the estimated amplitudes; the location of the hinges suggests the presence of pincer-like motions involving the two halves of the domain.

We speculate that the upper part might also be involved in some kind of binding event. We have noted previously the presence of a positively charged surface patch in the upper part [8] that might have some functional importance. Importantly, this patch is distinct from the previously described binding regions in the distantly related PH domains, where they interact with inositol phosphates [37]. In addition, Homer1 EVH1 does not bind to IP3 [5]. However, among the structures of related EVH1 domains, there are some examples showcasing a functional binding site in this region. The ENAH EVH1 binds a long PCARE peptide in this region, exhibits conformational changes specific for this extended ligand, and mutations in its $\beta4$-$\beta5$ loop considerably affect this interaction [38]. In the solution NMR structures of the N-WASP EVH1 domain fused to a partner polypeptide chain derived from WIP (PDB IDs: 2IFS and 1MKE), the contribution of multiple surface regions of the EVH1 domain to the recognition is also clearly apparent [39,40]. Notably, in both the ENAH EVH1:PCARE and the N-WASP EVH1:WIP complexes, the binding orientation of the partner peptide is the opposite of that in known Homer1 EVH1: partner complexes (Fig. S12).

Importantly, the presence of interactions outside the canonical binding site of Homer1 EVH1 is not supported by experimental data. Moreover, the actual biological effect of the mutations investigated in our work might be much more complex and might only be observable in the context of a larger protein complex building up the postsynaptic network. It should also be noted that although both mutations seem to perturb the internal motions, their effect is quite different and in several respects even opposite. Thus, it is by no means clear whether these two mutations, if they indeed contribute to the development of ASD as causative features, have comparable functional effects at the level of the postsynaptic protein network.

Acknowledgements

This work was supported by the Hungarian National Research, Development and Innovation Office (NKFIH) (grant nos.: OTKA K 137947, TKP2021-EGA-42, and 2021-4.1.2-NEMZ_KI-2022-00027). The research was also supported by the University of Debrecen, Scientific Research Bridging Fund (DETKA) and by the EU and cofinanced by the European Regional Development Fund under the projects GINOP-2.3.2-15-2016-00008 (G.B.) and GINOP-2.3.3-15-2016-00004 (access to Bruker NEO 700 MHz NMR spectrometer). We are grateful to CF Biomolecular Interactions and Crystallography of CIISB, Instruct-CZ Centre, supported by MEYS CR (LM2023042) and European Regional Development Fund (Project 'Innovation of Czech Infrastructure for Integrative Structural Biology', No. CZ.02.01.01/00/23_015/0008175). The authors thank Gitta Schlosser for the HPLC-MS measurements, and Viktor Farkas for the supervision of CD spectroscopy measurements. We acknowledge the Digital Government Development and Project Management Ltd. for awarding us access to the Komondor HPC facility based in Hungary.

Author contributions

ZG created the concept of the study. ZG and BP designed the methodology. FF, BM, ZEK, TK, GYB, and BP performed the experiments. FF, BM, ZEK, TK, GYB, BP, and ZG analyzed the data. ZEK and ZG performed molecular dynamics simulations. GYB, TK, and ZG provided funding and resources. ZG, FF, and ZEK wrote the original draft of the manuscript. ZG, FF, and ZEK created the figures and tables. BP and GYB made manuscript revisions.

Data accessibility

Chemical shifts have been deposited in the BMRB under accessions 53 479 (M65I) and 53 480 (S97L). SAXS data have been deposited in SASBDB under accessions SASDYW3 (M65I) and SASDYX3 (S97L). Ensembles from the molecular dynamics simulations

for the WT, M65I, and S97L variants are available at Zenodo (https://zenodo.org/records/17827462). The data contain PDB-format coordinate sets for the 3 parallel runs for each variant, with 501 total snapshots from the full 1 μs production runs.

References

1 Luo P, Li X, Fei Z and Poon W (2012) Scaffold protein Homer 1: implications for neurological diseases. *Neurochem Int* **61**, 731–738. doi: 10.1016/j.neuint.2012.06.014

2 Cheng D, Hoogenraad CC, Rush J, Ramm E, Schlager MA, Duong DM and Xu P (2006) Relative and absolute quantification of postsynaptic density proteome isolated from rat forebrain and cerebellum. *Mol Cell Proteomics* **5**, 1158–1170. doi: 10.1074/mcp.D500009-MCP200

3 Sheng M and Hoogenraad CC (2007) The postsynaptic architecture of excitatory synapses: a more quantitative view. *Annu Rev Biochem* **76**, 823–847. doi: 10.1146/annurev.biochem.76.060805.160029

4 Irie K, Nakatsu T, Mitsuoka K, Miyazawa A, Sobue K, Hiroaki Y, Doi T, Fujiyoshi Y and Kato H (2002) Crystal structure of the Homer 1 family conserved region reveals the interaction between the EVH1 domain and own proline-rich motif. *J Mol Biol* **318**, 1117–1126. doi: 10.1016/S0022-2836(02)00170-5

5 Beneken J, Tu JC, Xiao B, Nuriya M, Yuan JP, Worley PF and Leahy DJ (2000) Structure of the Homer EVH1 domain-peptide complex reveals a new twist in polyproline recognition. *Neuron* **26**, 143–154.

6 Shiraishi-Yamaguchi Y and Furuichi T (2007) The Homer family proteins. *Genome Biol* **8**, 206. doi: 10.1186/gb-2007-8-2-206

7 Ball LJ, Jarchau T, Oschkinat H and Walter U (2002) EVH1 domains: structure, function and interactions. *FEBS Lett* **513**, 45–52. doi: 10.1016/s0014-5793(01)03291-4

8 Kálmán ZE, Czajlik A, Maruzs B, Farkas F, Pap I, Homonnay C, Klumpler T, Batta G, Gáspári Z and Péterfia B (2026) Structural Modeling and Dynamics of the Full-Length Homer1 Multimer. *Proteins: Structure, Function, and Bioinformatics* **94**, 947–960.

9 Kim YE, Kim M, Kim S, Lee R, Ujihara Y, Marquez-Wilkins EM, Jiang YH, Yang E, Kim H, Lee C *et al.* (2025) Endothelial SHANK3 regulates tight junctions in the neonatal mouse blood-brain barrier through β-Catenin signaling. *Nat Commun* **16**, 1407.

10 Sheng M and Kim E (2000) The shank family of scaffold proteins. *J Cell Sci* **113**, 1851–1856. doi: 10.1242/jcs.113.11.1851

11 Sigar P, Kathrein N, Gragas E, Kupis L, Uddin LQ and Nomi JS (2025) Age-related changes in brain signal variability in autism spectrum disorder. *Mol Autism* **16**, 8.

12 Kelleher RJ III, Geigenmüller U, Hovhannisyan H, Trautman E, Pinard R, Rathmell B, Carpenter R and Margulies D (2012) High-throughput sequencing of mGluR signaling pathway genes reveals enrichment of rare variants in autism. *PLoS One* **7**, e35003.

13 Kelleher RJ and Bear MF (2008) The autistic neuron: troubled translation? *Cell* **135**, 401–406. doi: 10.1016/j.cell.2008.10.017

14 Fatemi SH, Eschenlauer A, Aman J, Folsom TD and Chekouo T (2024) Quantitative proteomics of dorsolateral prefrontal cortex reveals an early pattern of synaptic dysmaturation in children with idiopathic autism. *Cereb Cortex* **34**, 161–171.

15 Marley J, Lu M and Bracken C (2001) A method for efficient isotopic labeling of recombinant proteins. *J Biomol NMR* **20**, 71–75. doi: 10.1023/a:1011254402785

16 Studier FW (2014) Stable expression clones and auto-induction for protein production in E. Coli. *Methods Mol Biol* **1091**, 17–32. doi: 10.1007/978-1-62703-691-7_2

17 Huynh K and Partch CL (2015) Analysis of protein stability and ligand interactions by thermal shift assay. *Curr Protoc Protein Sci* **79**, 28–29.

18 Grudinin S, Garkavenko M and Kazennov A (2017) Pepsi-SAXS: an adaptive method for rapid and accurate computation of small-angle X-ray scattering profiles. *Acta Crystallogr D Struct Biol* **73**, 449–464. doi: 10.1107/S2059798317005745

19 Vranken WF, Boucher W, Stevens TJ, Fogh RH, Pajon A, Llinas M, Ulrich EL, Markley JL, Ionides J and Laue ED (2005) The CCPN data model for NMR spectroscopy: development of a software pipeline. *Proteins: Structure, Function, and Bioinformatics* **59**, 687–696.

20 Lee W, Tonelli M and Markley JL (2015) NMRFAM-SPARKY: enhanced software for biomolecular NMR spectroscopy. *Bioinformatics* **31**, 1325–1327.

21 Tamiola K, Acar B and Mulder FA (2010) Sequence-specific random coil chemical shifts of intrinsically disordered proteins. *J Am Chem Soc* **132**, 18000–18003.

22 Dudola D, Kovács B and Gáspári Z (2017) CoNSEnsX+ webserver for the analysis of protein structural ensembles reflecting experimentally determined internal dynamics. *J Chem Inf Model* **57**, 1728–1734.

23 Dosset P, Hus JC, Blackledge M and Marion D (2000) Efficient analysis of macromolecular rotational diffusion from heteronuclear relaxation data. *J Biomol NMR* **16**, 23–28.

24 Vallurupalli P, Bouvignies G and Kay LE (2012) Studying invisible excited protein states in slow exchange with a major state conformation. *J Am Chem Soc* **134**, 8148–8161.

25 Li D and Brüschweiler R (2025) COLMARvista: an open source 2D and pseudo-3D NMR spectral

processing, visualization, and analysis software in JavaScript. *J Biomol NMR* **79**, 171–179.
26 Delgado J, Reche R, Cianferoni D, Orlando G, van der Kant R, Rousseau F, Schymkowitz J and Serrano L (2025) FoldX force field revisited, an improved version. *Bioinformatics* **41**, p.btaf064.
27 Páll S, Zhmurov A, Bauer P, Abraham M, Lundborg M, Gray A, Hess B and Lindahl E (2020) Heterogeneous parallelization and acceleration of molecular dynamics simulations in GROMACS. *J Chem Phys* **153**.
28 Lindorff-Larsen K, Piana S, Palmo K, Maragakis P, Klepeis JL, Dror RO and Shaw DE (2010) Improved side-chain torsion potentials for the Amber ff99SB protein force field. *Proteins: Structure, Function, and Bioinformatics* **78**, 1950–1958.
29 Andersen CA, Bohr H and Brunak S (2001) Protein secondary structure: category assignment and predictability. *FEBS Lett* **507**, 6–10.
30 Clementel D, Del Conte A, Monzon AM, Camagni GF, Minervini G, Piovesan D and Tosatto SC (2022) RING 3.0: fast generation of probabilistic residue interaction networks from structural ensembles. *Nucleic Acids Res* **50**, W651–W656.
31 Zhang S, Krieger JM, Zhang Y, Kaya C, Kaynak B, Mikulska-Ruminska K, Doruker P, Li H and Bahar I (2021) ProDy 2.0: increased scale and scope after 10 years of protein dynamics modelling with Python. *Bioinformatics* **37**, 3657–3659.
32 Meng EC, Goddard TD, Pettersen EF, Couch GS, Pearson ZJ, Morris JH and Ferrin TE (2023) UCSF ChimeraX: Tools for structure building and analysis. *Protein Sci* **32**, e4792.
33 Paysan-Lafosse T, Blum M, Chuguransky S, Grego T, Pinto BL, Salazar GA, Bileschi ML, Bork P, Bridge A, Colwell L *et al.* (2023) InterPro in 2022. *Nucleic Acids Res* **51**, D418–D427.
34 Waterhouse AM, Procter JB, Martin DM, Clamp M and Barton GJ (2009) Jalview Version 2—a multiple sequence alignment editor and analysis workbench. *Bioinformatics* **25**, 1189–1191.
35 Sievers F and Higgins DG (2014) Clustal omega. *Curr Protoc Bioinformatics* **48**, 3–13.
36 Altenhoff AM, Warwick Vesztrocy A, Bernard C, Train CM, Nicheperovich A, Prieto Baños S, Julca I, Moi D, Nevers Y, Majidian S *et al.* (2024) OMA orthology in 2024: improved prokaryote coverage, ancestral and extant GO enrichment, a revamped synteny viewer and more in the OMA Ecosystem. *Nucleic Acids Res* **52**, D513–D521.
37 Anand K, Maeda K and Gavin A-C (2012) Structural analyses of the Slm1-PH domain demonstrate ligand binding in the non-canonical site. *PLoS One* **7**, e36526. doi: 10.1371/journal.pone.0036526
38 Hwang T, Parker SS, Hill SM, Ilunga MW, Grant RA, Mouneimne G and Keating AE (2021) A distributed residue network permits conformational binding specificity in a conserved family of. *eLIFE J* **10**.
39 Volkman BF, Prehoda KE, Scott JA, Peterson FC and Lim WA (2002) Structure of the N-WASP EVH1 domain-WIP complex: insight into the molecular basis of Wiskott-Aldrich syndrome. *Cell* **111**, 565–576. doi: 10.1016/s0092-8674(02)01076-0
40 Peterson FC, Deng Q, Zettl M, Prehoda KE, Lim WA, Way M and Volkman BF (2007) Multiple WASP-interacting protein recognition motifs are required for a functional interaction with N-WASP. *J Biol Chem* **282**, 8446–8453. doi: 10.1074/jbc.M609902200

Supporting information

Additional supporting information may be found online in the Supporting Information section at the end of the article.

Fig. S1. Amide NH chemical shift perturbations of the mutants compared with the wild-type domain and NH-NH NOEs characteristic of the EVH1 fold, observed in the M65I variant.

Fig. S2. Structural models colored according to the chemical shift perturbations and comparison of selected side chains in the WT and M65I variants.

Fig. S3. Overlaid 1H-15 N HSQC spectra during the titration for the three variants.

Fig. S4. Amide NH chemical shift perturbations upon ligand binding for the three variants.

Fig. S5. R1, R2 relaxation and hetNOE data for the M65I mutant.

Fig. S6. R1, R2 relaxation and hetNOE data for the S97L mutant.

Fig. S7. Amide S2 order parameters depicted separately for the three domain variants investigated.

Fig. S8. R_{ex} contributions depicted separately for the three domain variants investigated.

Fig. S9. Per-residue RMSF values of the wild-type and mutant structures observed during the 1 us simulations.

Fig. S10. Ensembles showing the MD snapshots for the WT and variant EVH1 domains.

Fig. S11. Sequence alignments of EVH1 domains highlighting the variability of the positions affected by the mutations investigated in this study.

Fig. S12. Examples of EVH1 domains with extended binding sites. The binding of longer peptide segments affects the conformation of the β5-β6 loop. See text for details. Figure prepared with ChimeraX.